Carbon 173 (2021) 953–967

Contents lists available at ScienceDirect

Carbon

journal homepage: www.elsevier.com/locate/carbon

Research Article

Spatial distribution of metallic heteroatoms in soot nanostructure mapped by aberration-corrected STEM-EELS

Henrik Wiinikka [a, b, *], Fredrik S. Hage [c, d], Quentin M. Ramasse [c, e], Pal Toth [a, f]

[a] RISE Energy Technology Center, Box 726, SE 941 28, Piteå, Sweden
[b] Division of Energy Science, Department of Engineering Sciences and Mathematics, Luleå University of Technology, SE-97187, Luleå, Sweden
[c] SuperSTEM Laboratory, SciTech Daresbury Campus, Daresbury, WA4 4AD, United Kingdom
[d] Department of Materials, University of Oxford, Oxford, OX1 3PH, United Kingdom
[e] School of Chemical and Process Engineering and School of Physics and Astronomy, University of Leeds, Leeds, LS2 9JT, United Kingdom
[f] University of Miskolc, Institute of Physical Metallurgy, Metalforming and Nanotechnology, Miskolc-Egyetemvaros, 3515, Miskolc, Hungary

ARTICLE INFO

Article history:
Received 14 September 2020
Received in revised form
9 November 2020
Accepted 2 December 2020
Available online 4 December 2020

Keywords:
Soot
STEM-EELS
Graphite structure
Carbon-oxygen functional groups
Oxidation

ABSTRACT

Soot from the thermochemical conversion of solid and liquid fuels can be infused with metallic heteroatoms originating from the fuel – these heteroatoms alter the nanostructure and the reactivity of the soot. Here, we investigate the spatial distribution of metallic heteroatoms in soot generated by biomass gasification, using aberration-corrected Scanning Transmission Electron Microscopy and Electron Energy Loss Spectroscopy (STEM-EELS). The technique allowed for the mapping of heteroatom distribution in soot at the nanoscale, and thereby for the direct correlation of heteroatom concentration with the graphitic nanostructure. Spherical soot particles were coated with a thin layer of silicon, possibly in the form of quartz that may be linked to minor distortions of the nanostructure of the graphitic shell of the particles. Further results on non-spherical soot and inorganic-carbon fused aggregates suggest that the chemistry of formation was affected by the presence of gaseous ash-forming elements, especially calcium, with carbon-oxygen functional groups forming as intermediates in the graphite-inorganic reaction; i.e., prior to the formation of the thermodynamically stable carbonate bonds. The analytical approach demonstrated here can potentially help select fuel additives or aid in the design of fuel blends that minimize the formation of similar, hybrid carbon nanoparticles in combustion or gasification systems.

1. Introduction

Soot is an unwanted byproduct of thermochemical conversion processes – combustion, gasification and pyrolysis. The formation of soot reduces the efficiency of thermochemical conversion processes and can cause technical problems; e.g., deposit formation in furnaces and reactors [1,2] and ignition problems in engines [3]. As an air pollutant, often called black carbon [4], soot negatively affects air quality [5], human health [6] and contributes to global warming [7]. Because of these adverse properties, it is important to minimize the emission of soot during the thermochemical conversion of carbonaceous feedstocks, either by combustion optimization or downstream gas cleaning. However, in other industrial processes, the production of soot-like carbonaceous nanoparticles [8] should be maximized – as in the case of, e.g., Carbon Black (C.A.S. no 1333-86-4), one of the top 50 industrial chemicals, with a global production of 13 Mt in 2015 [9]. Soot is formed at high temperature in fuel-rich hydrocarbon flames [10]. Soot is an aerosol, containing primary particles with typical diameters of 30–500 nm that consist of concentrically stacked graphene layers with various degrees of disorder (so-called turbostratic carbon), often arranged in a core-shell structure [11]. The nanostructure of the particles affects their conversion; e.g., the oxidation rate of pure carbon soot depends on the nanostructure, and soot with amorphous and less ordered structures display higher reactivity compared to soot with more ordered, graphitic structures [12–15]. For Carbon Black, the nanostructure is also important from the perspective of the performance of the material, particularly as a functional material in energy storage, conversion, and harvesting applications [16,17].

* Corresponding author. RISE Energy Technology Center, Box 726, SE 941 28, Piteå, Sweden.
E-mail address: henrik.wiinikka@ri.se (H. Wiinikka).

https://doi.org/10.1016/j.carbon.2020.12.004

Many practically relevant liquid and solid fuels contain metals or ash-forming elements – soot formed during the combustion of these fuels can therefore be infused with varying amounts of trace metals [18–24]. Compared to pure hydrocarbon flames, the formation of soot in environments that contain gaseous metals is less investigated and understood. Metal additives [26], especially alkali elements [27–30] are known to suppress soot formation in flames and to catalyze soot oxidation in diesel particle filters [31]. Iron additives are also known to affect the morphology and oxidation behavior of diesel soot [32]. In Carbon Black production, potassium salt additives are used to control the properties of the produced particles [8]. In biomass gasification or high-temperature pyrolysis, the introduction of alkalis through the fuel, or as an additive, has also been shown to significantly decrease the production of soot [33–35]. Interestingly, a study of metal-infused soot particles produced in a real gasification environment [36] found that higher reactor temperatures resulted in less ordered nanostructure and higher reactivity; i.e., metal-infused soot followed the opposite trend of that observed in the case of pure carbon soot [12–15]. Higher reactivity of soot generated in the high-temperature pyrolysis of ash-rich biomass has also been observed [33] and there is a strong indication that ash-forming elements in high-temperature processes affect both the nanostructure and reactivity of biomass-based soot. Information of how the metals are distributed in the soot particle and any associated effects on the graphitic nanostructure is of great importance for understanding particle formation mechanisms.

Compared to bulk analysis methods such as powder X-ray diffractometry (XRD), Raman microspectrometry and X-ray absorption spectroscopy, High Resolution Transmission Electron Microscopy (HRTEM), often in combination with digital image analysis, is the preferred tool for analyzing the nanostructure of individual soot particles [37]. Combined with energy dispersive X-ray spectroscopy (EDS), the technique also provides information about the elemental composition of metal-infused soot particles [25,36]. While elemental analysis down to atomic resolution is possible with EDS in the electron microscope, using aberration-corrected Scanning Transmission Electron Microscopy (STEM) [38,39], (S)TEM-EDS cannot provide information on the chemical state and types of atomic bonds in the particles. Electron Energy Loss Spectroscopy (EELS) [40,41] however, has the potential to provide this information – in combination with aberration corrected STEM, this allows for atomically resolved imaging and chemical mapping of, e.g., thin crystalline or 2D materials [42–47] and 1D nanostructures [48,49].

The analysis of turbostratic soot particles is more challenging than that of 2D materials or crystalline nanostructures due to the (often disordered) 3D structure of the particle. HRTEM-EELS and STEM-EELS have previously been used to study the structural changes of soot during low temperature oxidation [50,51]. Recently, the maturation of pure soot particles sampled along the axis of a laboratory-scale CH_4 flame has been investigated with HRTEM-EELS and aberration corrected STEM-EELS by analyzing the carbon hybridization (sp^2/sp^3 ratio) in the soot [52]. However, to the best of our knowledge.

(i) metal-containing soot particles have not been analyzed before with aberration corrected STEM-EELS and
(ii) the mapping of chemical and structural information obtained from spatially resolved, aberration corrected STEM-EELS of soot has not been reported.

In this work, different types of metal-containing soot particles, pre-scanned with HRTEM-EDS [36], were analyzed using a dedicated aberration-corrected STEM-EELS instrument (Nion UltraSTEM 100). In order to reduce potential beam damage to the samples [52], the microscope was operated at an acceleration voltage of 60 kV, which is below the knock-on-damage of single layer of defect free graphene [53].

The objective of this work was to:

(i) demonstrate that aberration corrected STEM-EELS is applicable for analyzing metal-containing soot particles,
(ii) obtain spatially resolved information about the distribution of elements and nanostructure,
(iii) map the chemical structure (bonding) of the particles, and
(iv) contribute to the understanding of the complex soot formation process in environments that contain gaseous metal species.

2. Material and methods

2.1. Soot generation and sampling

Soot particles were generated in high-temperature, pressurized, oxygen-blown, entrained flow gasification of wood powder. This is the preferred gasification technology for generating high-quality syngas from biomass (rich in CO, H_2 and low in CH_4 with no tar content) that can be further upgraded to renewable motor- or aviation fuels in a downstream synthesis plant [54]. A detailed description of the gasifier [55], feedstock and experimental conditions [36,56], and particle sampling [36] were given elsewhere and is therefore only briefly summarized here. The absolute pressure of the top-fired gasifier was 7 bar and the feed rate of wood powder corresponded to a thermal load of 0.6 MW. The composition of the wood powder adopted from Ref. [36] is presented in Table 1. The process temperature of the reactor, as measured by *S*-Type thermocouples, was controlled by the amount of oxygen supplied, and varied from 1119 °C to above 1550 °C. Particle sampling was performed in the raw syngas pipe (temperature

Table 1
Physical and chemical composition of the fuel [36].

Particle size distribution (μm)	
d_{50}	140
d_{90}	240
Proximate analysis (wt.%, as received)	
Moisture	7.7
Volatile	77.9
Fixed carbon	14.0
Ash	0.34
Ultimate analysis (wt.%, dry)	
C	51.3
H	6.4
N	<0.10
Cl	<0.02
S	0.02
O (by differences)	41.8
Major ash forming elements (mg/kg, dry)	
Si	28
Al	12
Ca	979
Fe	8
K	389
Mg	149
Mn	91
Na	40
P	34
Zn	7

60–100 °C) after the quench section of the gasifier and the particles in the raw syngas were separated from the gas stream by a Teflon filter. The filter holder was heated to avoid water condensation. Particles from the filter were mechanically transferred onto a lacey amorphous carbon support film on copper TEM grids (Ted Pella).

2.2. Investigated soot samples

Four different samples, collected at process temperatures of 1119 °C, 1313 °C, 1430 °C, and 1550 °C were investigated by aberration corrected STEM-EELS. The overall morphology and elemental composition of the investigated particles were previously analyzed by scanning electron microscopy (SEM, Zeiss Merlin FEG-SEM) [36], and transmission electron microscopy (TEM, Jeol JEM 2100 F) equipped with an energy-dispersive X-ray spectrometer (EDS, JED 2300) – results on overall morphology and composition of particles are presented in Fig. 1. A detailed description of the particles can be found elsewhere [36]; here, only a short summary is given. At low process temperatures (1119 °C and 1313 °C), near-spherical soot particles dominated the samples and the overall carbon content was very high (above 97 wt.-%). As the process temperature increased, the morphology changed to non-spherical, irregular and angular shapes, while at the same time fused, carbon-inorganic agglomerates with some intermixed soot appeared. The overall metal content of the samples increased significantly and at the highest process temperature, the overall carbon content was reduced to less than 40 wt%.

Particles from the TEM grids have been classified based on their overall morphology and nanostructure as young soot, core-shell soot, hollow core-shell soot, large soot particles, non-spherical soot particles, highly oxidized soot particles, and finally, carbon-inorganic fused agglomerates. The classification was necessary due to the time-consuming nature of aberration corrected STEM-EELS analysis – for each process temperature, only a few particles were selected for analysis. Although it is impossible to claim with absolute certainty that our results are fully representative of the system as a whole, the care and extent of our analysis give us confidence they are as representative as can be of the sample studied under the electron beam. The classification of particles, their morphology and the number of particles analyzed for each process temperature are summarized in Fig. 2.

2.3. STEM-EELS

STEM-EELS data were acquired using a Nion UltraSTEM100 dedicated aberration corrected STEM, equipped with a Gatan Enfina EEL spectrometer. The microscope has a source energy spread of 0.35 eV. The microscope was operated at an acceleration voltage of 60 kV, using a 31 mrad convergence half-angle. This results in an effective electron probe size of about 1 Å.

The spectrometer collection half-angle was 36 mrad, the bright field (BF) detector angular range was 0–8 mrad while that of the high-angle annular-dark-field (HAADF) detector was 89–195 mrad. Spectrum acquisition times ranged from 0.05 s to 0.3 s, with an energy dispersion of 0.5 eV per channel, using full spectrum binning in the non-energy dispersive direction. STEM-EEL spectrum images were de-noised using principal component analysis (PCA) as implemented in the MSA plugin [57] for Gatan's Digital Micrograph suite (commercially available from HREM research [58]). Elemental maps of the silicon $L_{2,3}$, carbon *K* and oxygen *K* edges were generated by integrating the signal over a window up to 50 eV wide, from each ionization edge onset, subsequent to

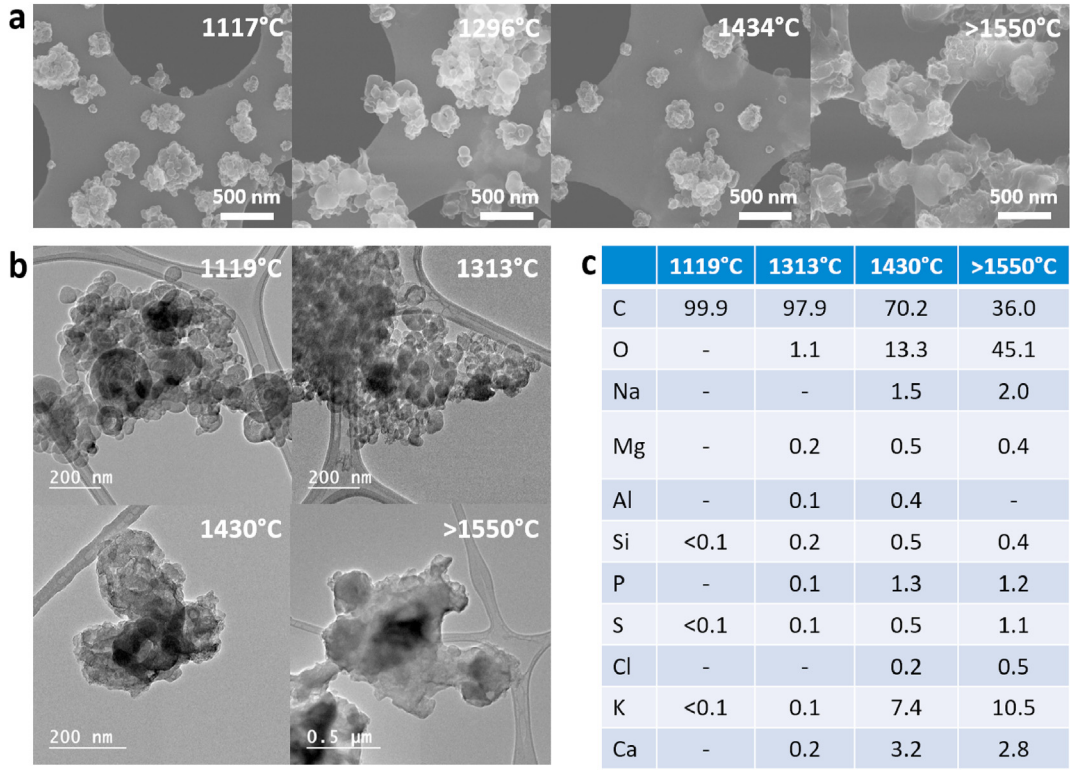

c

	1119°C	1313°C	1430°C	>1550°C
C	99.9	97.9	70.2	36.0
O	-	1.1	13.3	45.1
Na	-	-	1.5	2.0
Mg	-	0.2	0.5	0.4
Al	-	0.1	0.4	-
Si	<0.1	0.2	0.5	0.4
P	-	0.1	1.3	1.2
S	<0.1	0.1	0.5	1.1
Cl	-	-	0.2	0.5
K	<0.1	0.1	7.4	10.5
Ca	-	0.2	3.2	2.8

Fig. 1. Overall morphology and elemental composition of the investigated particles. (a) SEM micrographs. **(b)** Phase contrast TEM images, and **(c)** elemental composition (wt.%) analyzed with EDS of the particle agglomerates in **b**. Although the operating conditions of the gasifier was the same, there were a small difference in resulting process temperature when the particle sampling was performed between the corresponding particle samples (1117°C–1119 °C; 1296°C–1313 °C; 1434°C–1430 °C; and >1550°C->1550 °C) used for SEM and TEM analysis, see Ref. [34] for experimental details. (A colour version of this figure can be viewed online.)

a Type	1119°C	1313°C	1430°C	1550°C	Comment
Soot: young	1				TEM: Fig. 2b STEM: Fig. S3
Soot: core-shell	1	2			TEM: Fig. 2c STEM: Fig. S4
Soot: hollow core-shell		1	1		TEM: Fig. 2d STEM: Fig. 3
Soot: large particles	1				TEM: Fig. 2e STEM: Fig. S5
Soot: non-spherical		2			TEM: Fig. 2f STEM: Fig. 4
Soot: highly oxidized			1		TEM: Fig 2g STEM: Fig. 5
Carbon - inorganic fused agglomerates			1	2	TEM: Fig 2h and 2i STEM: Fig. 6

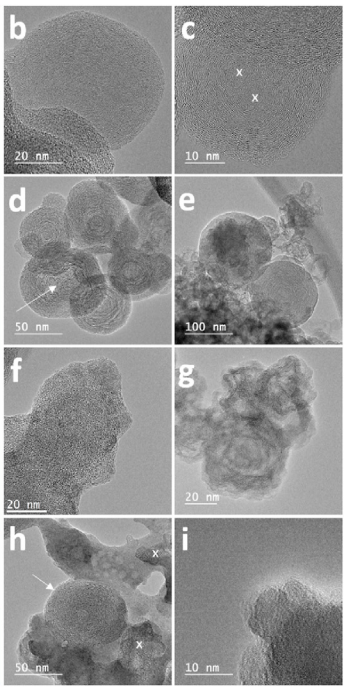

Fig. 2. Classification and morphology of investigated particles. **(a)** Description of how many particles that was investigated with STEM for each process temperature and where the results can be found. **(b–i)** Phase contrast TEM images of the different particle classes. **(b)**Young spherical soot particle. **(c)** Core-shell soot particles where the core consists of two nuclei which center is marked with crosses. **(d)** Hollow-core soot particles, the empty center is marked with an arrow for one particle. **(e)** Two large soot particles (primary particle diameter >100 nm) in the center of the images. Non-spherical and oxidized non spherical soot particle can also be seen in the upper right corner. **(f)** Non-spherical soot particle. **(g)** Highly oxidized non-spherical soot particles. **(h)** Carbon-inorganic fused agglomerates with intermixed soot particles (arrow and crosses). The arrow shows a large soot particle. **(i)** Inorganic rich particles in carbon-fused agglomerates. (A colour version of this figure can be viewed online.)

background subtraction using a power law function. Integration windows for the phosphorous $L_{2,3}$ and calcium $L_{2,3}$ edges were 15 and 12 eV wide, respectively. Special care was taken for cases where the carbon *K* and potassium $L_{2,3}$ edges were overlapping: the 11–12 eV carbon *K* integration window width was chosen to minimize the influence of the potassium $L_{2,3}$ on the resulting carbon maps. So-called "ratio maps" of the silicon $L_{2,3}$, phosphorous $L_{2,3}$, calcium $L_{2,3}$ and oxygen *K* edges were generated by normalizing these to corresponding carbon *K* maps (11 eV integration window). Gaussian fitting routines based on refs. [59–62] were used to extract the spatial distribution (ratio maps) of potassium as well as that of graphitic and non-graphitic carbon; the routines were tailored to each dataset. Based on refs. [59–62], fitted peaks were attributed to: C=C π* (~285 eV), "a-peak": carbonyl (~286.5 eV), "b-peak": carboxyl (~288 eV), "c-peak": carbonate (~290 eV), C–C σ* (~292 eV), K L_3 (~297 eV) and L_2 (~300 eV) and, C=C σ* (~301 eV). For the dataset shown in Fig. 5, there is a lack of distinct peaks clearly attributable to carbonyl (~286.5 eV), carboxyl (~288 eV) or carbonate (~290 eV) presence. We therefore fit a single peak at ≈287 eV, capturing the extended tail of the graphitic π* signal as well as signal arising from carbon bonding with hetero-elements (including possible C–H bonds) and/or "fullerenic" non-planar sp^2 carbon bonding (see Zhang et al. [59], Mironov et al. [61] and references therein). C=C π*, carbonyl, carboxyl, carbonate and C–C σ* ratio maps were generated by normalizing to the total intensity of the carbon *K* edge (11 eV window), to minimize the contribution of the potassium $L_{2,3}$ signal. The fitted potassium L_3 and L_2 peak maps were extracted, summed and normalized to a map of the combined potassium $L_{2,3}$ and carbon *K* signal; the window integration width was here limited to 20 eV to minimize the contribution of plural scattering. For the dataset shown in Fig. 3, the oxygen/silicon content (at.-%) ratio of the outer particle "shell" was determined by means of relative quantification, using the silicon $L_{2,3}$, carbon *K* and oxygen *K* edges, fitting Hartree-Slater cross sections (including the ELNES) and subtracting the background using a power law. While the spectra were not deconvoluted for thickness, all observed regions were at the edges of the particles (thus it is reasonable to assume these regions are fairly thin), meaning that we estimate at most a minor contribution of plural scattering here. A conservative upper bound for possible errors in elemental concentrations extracted from EEL spectra can be estimated to be ±10%. Gaussian peak fitting and relative quantification were both carried out using the Gatan Microscopy Suite (GMS) 3 software.

2.4. Quantitative nanostructure analysis

The quantitative analysis of relationships between carbon nanostructure and heteroatom content – silicon in particular – was carried out using the image analysis framework of Toth et al. [63,64]. Since this framework is suitable for the analysis of microcrystalline carbon, only STEM images that contained visible fringes (i.e. image contrast attributable to individual graphene layers) were used for quantitative analysis. From the images, the interlayer spacing of graphite-like structures (d_{002}), two symmetry parameters, the polar and nematic symmetry strength (S_{2P} and S_{2N}, respectively), and the conventional fringe length and fringe tortuosity were extracted. The magnitude of interlayer spacing characterizes graphite-like microcrystals in soot: d_{002} in mature soot tends to be close to that in graphite (0.335 nm), while young soot and distressed, heavily oxidized structures tend to be characterized by longer d_{002} [63,65]. The symmetry parameters were originally introduced by Shim et al. [66] for the analysis of coal and char nanostructure. These parameters are higher-order statistics of fringe orientation. In brief, S_{2P} is bounded between −1 and 1; the value −1 corresponds to a perfectly radial arrangement of fringes,

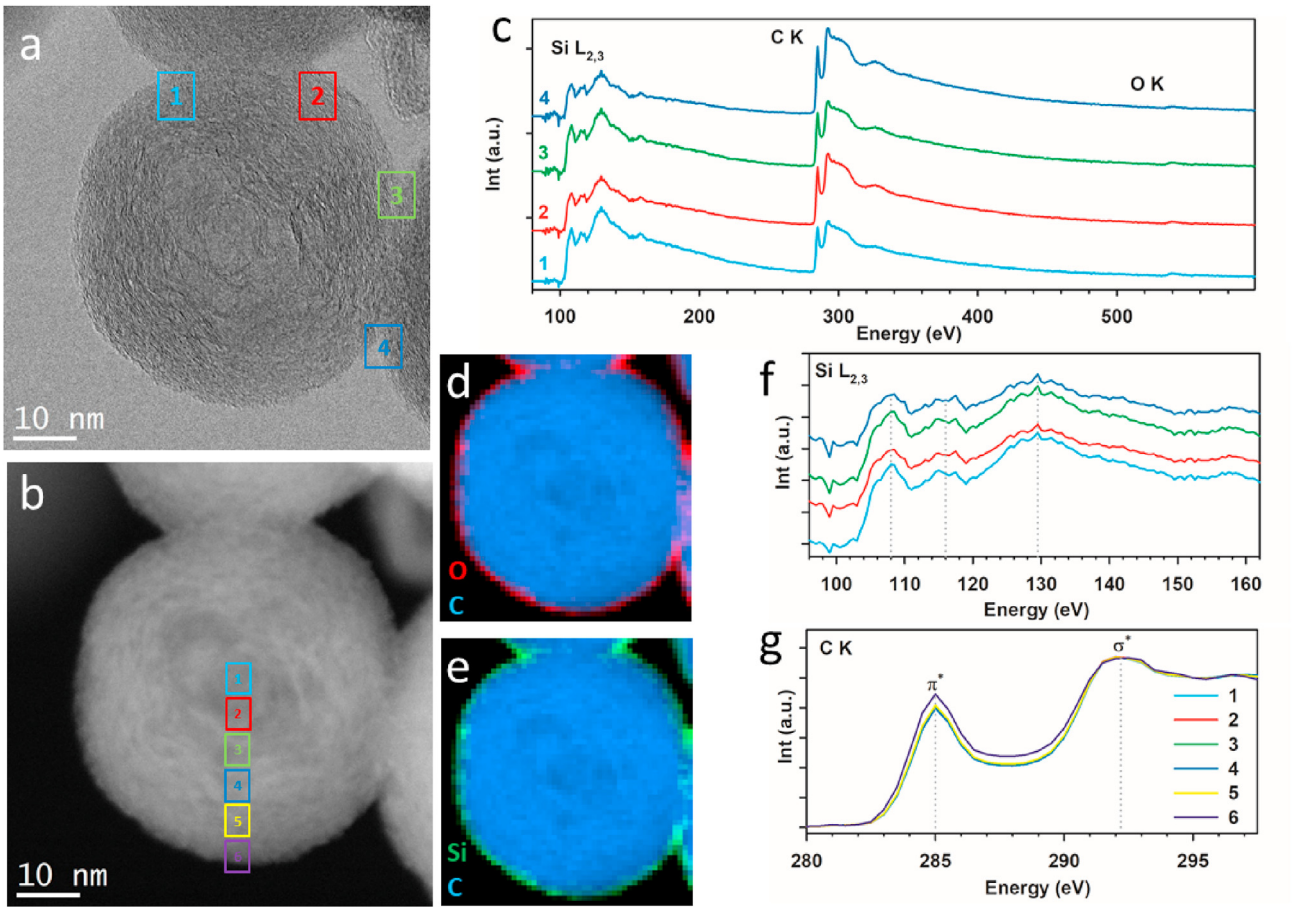

Fig. 3. STEM-EELS analysis of hollow core-shell soot. **(a)** BF-STEM image; **(b)** HAADF-STEM image; **(c)** Overview EELS signal from the areas marked in **a** showing the silicon $L_{2,3}$ edge (99 eV), carbon *K* edge (285 eV) and the oxygen *K* edge (532 eV); **(d–e)** Composite EELS maps of the particle, **(d)** oxygen and carbon, and **(e)** silicon and carbon. The corresponding EELS elemental map of carbon, oxygen and silicon to create the composite maps can be found in Figure S5. **(f)** ELNES of the silicon $L_{2,3}$ edge from the areas marked in **a**. **(g)** ELNES of the carbon K edge from the areas marked in **b**. The reactor temperature was 1313 °C. (A colour version of this figure can be viewed online.)

while a value of 1 corresponds to perfectly concentric fringes. The parameter S_{2N} is bounded between 0 and 1. The value 0 corresponds to a perfectly random fringe orientation, while a value of 1 corresponds to perfectly parallel fringes. It is important to note that symmetry parameters have a characteristic scale – this scale is the easiest to picture as the size of a neighborhood within which the fringes are analyzed. Consequently, a high S_{2N} value at a large scale indicates that fringes are directed along a single orientation and this orientation is maintained over long distances in the sample. Similarly, e.g. high polar symmetry over medium scales indicate that concentric rings of fringes are seen in the sample and that the size of these rings is approximately that of the said medium scale. An explanatory figure that demonstrates the concept of multiscale symmetry can be seen in the Supplementary Material (Fig. S1). Fringe length and tortuosity are standard parameters for the analysis of carbon nanostructure [67] – longer fringes signify a more ordered structure that is subsequently less reactive due to the lower availability of edge-site carbon atoms; fringe tortuosity is a measure of the curvature of the carbon lamellae that is indicative of ring strain within the structure.

High-resolution STEM-EELS analysis allowed for the joint analysis of carbon nanostructure and elemental composition – specifically the spatial distribution of silicon – and the carbon nanostructure. Besides carbon and oxygen, silicon was the only element originating from the fuel ash that could be detected and mapped within particles that were crystalline enough for nanostructure characterization and was therefore deemed as the only heteroatom relevant for further analysis. Via the registration of STEM images and EELS elemental maps, it was possible to correlate structural parameters and elemental composition at the native image resolution: i.e., at every pixel. Similar data were previously not available to the research community; as such, work presented in this paper is, to our knowledge, the first that demonstrates structure-composition relationships natively at the nanoscale. Image registration was carried out manually, via aligning recognizable features in the STEM images and EELS maps. An example of aligned STEM and EELS data is shown in Fig. S2.

3. Results and discussion

3.1. Spherical soot particles

Fig. 3 presents results from STEM-EELS analysis of hollow core-shell soot particles. The results of comparable analysis of young soot, core-shell soot, and large soot particles are shown in Figs S3 – S5 in the Supplementary Material. The differences in nanostructure between these three particle classes, easily observed in the BF-STEM images (see Fig. 3a, and Figs S3a and S4a), is due to maturation and oxidation of the soot particles [11]. After young soot transformed to core-shell particles, oxidation became selective to the more reactive amorphous core, leading to the hollowing of the particle cores. The progress of oxidation, from start-to-finish, has recently been visualized in real-time using in-situ high-resolution TEM, confirming hypotheses based on ex-situ investigations [68].

The hollow core is also easily visualized by HAADF-STEM (see Fig. 3b). Using EELS, silicon, carbon, and oxygen can be detected in the particles (see Fig. 3c, and Figs S3c and S4c). Composite EELS maps of oxygen and carbon (Fig. 3d, and Figs S3g-S4g) and silicon and carbon (Fig. 3e, Figs S3h-S4h) show that silicon and oxygen are concentrated in a thin layer (1–2 nm) close to the surface of spherical soot particles. Corresponding elemental carbon, oxygen and silicon EELS maps used to produce results shown in Fig. 3 are shown in Fig. S6). Also, large soot particles have a layer of silicon and oxygen at their surface (Fig. S5). Interestingly, oxygen enrichment was observed at "neck-sites", connecting primary particles – this can be taken as an indication of preferential oxidation [69]; i.e., oxidation of soot occurring at the "bridges" connecting particles in the agglomerate, eventually leading to agglomerate fragmentation [70,71].

The corresponding silicon $L_{2,3}$ edge and carbon *K* edge Energy Loss Near Edge fine Structure (ELNES) is presented in Fig. 3f–g. Silicon $L_{2,3}$ peaks at ~104 eV, ~108 eV and 116 eV, accompanied by broader peak at ~130 eV was fairly consistent with the ELNES of SiO_2 (quartz) reported by Garvie et al., [72]. However, based on only the ELNES we cannot rule out the presence of a small amount of elemental silicon in the samples. All carbon *K* edge spectra (Fig. 3g, Figs S3j, S4j, and S5j) show that the particle was graphitic [73], i.e., predominantly sp^2 bonded. Taking into account spectral noise, no significant change in π* or σ* broadening was observed in the spectra sampled radially from the center towards the edge of the particle; significant broadening of these peaks would be indicative of a decrease in graphitic order (i.e. degree of sp^2 hybridization). An increase in relative π* intensity at the edge was most likely due to an abrupt change in the average orientation of graphene layers at and near the surface (i.e. due to the overall spherical particle geometry), not due to a change in the sp^2 content [73]. Due to the anisotropy of the graphitic structure, meaningful extraction of sp^2 content using carbon *K* edge intensities requires careful consideration of electron beam and sample geometries (during both data acquisition and analysis); highly specific experimental beam geometries are often needed [73,74]. This was deemed beyond the scope of the present work. Furthermore, judging from the ELNES signal the presence of SiO_2 in the near-edge region of the particle did not appear to noticeably affect the graphitic structure of the soot particle, within experimental resolution and noise.

The bulk elemental composition (Fig. 1C) of silicon and oxygen in these particles were very low, below 1 wt-% [36]; however, it was still possible to detect these elements by STEM-EELS, due to the fact that silicon and oxygen were enriched on the particle surface - the concentration of silicon and oxygen here were ~9–19 wt-% and ~10–18 wt-%, respectively (see Fig. S7). Furthermore, the atomic ratio between oxygen and silicon was approximately 2 on the surface, indicating the presence of SiO_2 and furthermore, that the contribution from elemental silicon in comparison to SiO_2 is much lower. EDS analysis revealed that the soot particles also contained traces of potassium (see Fig. 1C); in the EELS spectra, any potassium $L_{2,3}$ peaks at 299 eV and 297 eV were most likely obscured by the relative intense carbon *K* edge σ* peak at ~292 eV, suggesting that potassium may be more evenly distributed throughout the particles compared to silicon and oxygen.

3.2. Non-spherical soot particles

Results from STEM-EELS analysis of a non-spherical soot particle are presented in Fig. 4 and Fig. S8. The BF-STEM images seen in Fig. 4a, and Fig. S8a, revealed no periodic fringes, indicative of a mostly amorphous structure. The HAADF-STEM images (Fig. 4b, and Fig. S8b) of the particle had a uniform contrast. Using EELS (Fig. 4c, and Fig. S8c), carbon, potassium, calcium, oxygen and possibly traces of manganese could be detected. No significant amount of silicon was detected, either at the surface or in the interior of the particle.

The ELNES of the carbon *K* edge, potassium $L_{2,3}$ edge, calcium $L_{2,3}$ edge and the oxygen *K* edge extracted from different regions of the particle are presented in Fig. 4d and Fig. S8d. Close to the surface of the particle, the fine structure of the carbon *K* edge – including the π* and σ* peaks (at 285 eV and 292eV, respectively) – was indicative of a graphitic structure and suggested the presence of graphitic crystalline fragments on the very edge of the particles. Superimposed on the σ* peak, at slightly higher energy loss, the potassium $L_{2,3}$ peaks were seen (~300 eV and ~297 eV). At the center of the particle, two additional carbon *K* edge peaks, located at ~286.5 eV and at ~288 eV (energy loss between the graphitic π* and σ* peaks), were clearly present, marked "a" and "b" in Fig. 4d. Simultaneously, the intensity of the potassium $L_{2,3}$ peak increased relative to the carbon *K* edge, indicating an increase in potassium content.

For the data presented in Fig. 4d, the overall ELNES profile could be approximated by means of fitting Gaussian functions to the aforementioned peaks (see Fig. S9a). However, for the data presented in Fig. S8d, another peak (marked "c") at 290 eV must be added to the Gaussian fitting routine in order to fully explain the shape of the ELNES profile (see Fig. S9b). The two (a and b) or three (a, b, and c) extra peaks in the carbon *K* edge indicated a more complex, non-graphitized carbon structure at the center of the particle, consistent with BF-STEM results. However, unambiguous attribution of the ~286.5 eV and ~288 eV peaks to specific chemical bonds is not trivial. Both EELS and synchrotron techniques, i.e., X-ray absorption near-edge structure (XANES) or scanning transmission X-ray microscopy (STXM), have shown that different functional groups from a variety of carbon-based samples (e.g. diesel soot [75], aircraft soot [76], and organic-containing meteorites [77–79]) display peaks in this energy range: aromatic/olefin rings at ~285 eV, aromatic aldehyde/keton at 286.3–286.8 eV, aliphatic bonds at 287.2–288.3 eV, and finally, carboxyl bonds at 288.5–288.7 eV. Additionally, carbonate bonds give a peak at ~290 eV [72,80]. Furthermore, different types of fullerenes (e.g. C_{60}, $C_{59}N$, K_3C_{60}, K_6C_{60}) also generate multiple peaks between 282 and 295 eV, e.g., peaks at ~284.5 eV, ~286 eV, ~288 eV, and minor peaks at ~291 eV and ~293 eV [81–83]; flame synthesis is one of the production methods for C_{60} and C_{70} fullerenes [84]. Furthermore, based on HRTEM imaging, Grieco et al. [85], concluded that non-spherical soot particles consist of fullerenic carbon. In-situ HRTEM has also shown that fullerenes can be formed at the surface of a burning soot particle [68]. All these reports clearly show that there are many candidate structures for assigning to the ~286.5 eV, ~288 eV, and ~290 eV peaks. However, because there seems to be a correlation between the intensity of these three extra peaks and the intensity of the heteroatoms (K, Ca and O) in the EELS signal, the most likely attribution is a carbon-oxygen bonding environment, with peaks a and b representing different carbonyl bonds: i.e. peak an at ~286.5 eV is due to ketone bonds (C=O), and not aldehyde bonds (O=CH); and peak b at ~288 eV is due to carboxyl bonds (O=C–O). Finally, peak c at ~290 eV can be attributed a carbonate bonding (CO_3^{2-}) environment.

The ELNES of the calcium $L_{2,3}$ edge is characterized by two main peaks at ~348.5 eV and ~352 eV. Considering the noise level, no minor pre-peaks that could indicate carbonate bonds could be detected. Minor pre-peaks on the low energy side of both the calcium L_3 and L_2 peaks have been previously identified in XANES of calcite ($CaCO_3$) [86]. The ELNES of the oxygen *K* edge showed a main peak at ~541 eV and a pre-peak at ~535 eV for the spectra extracted from the central parts of the particle where the latter could be an indication of both carboxylic acid functional groups [87] or

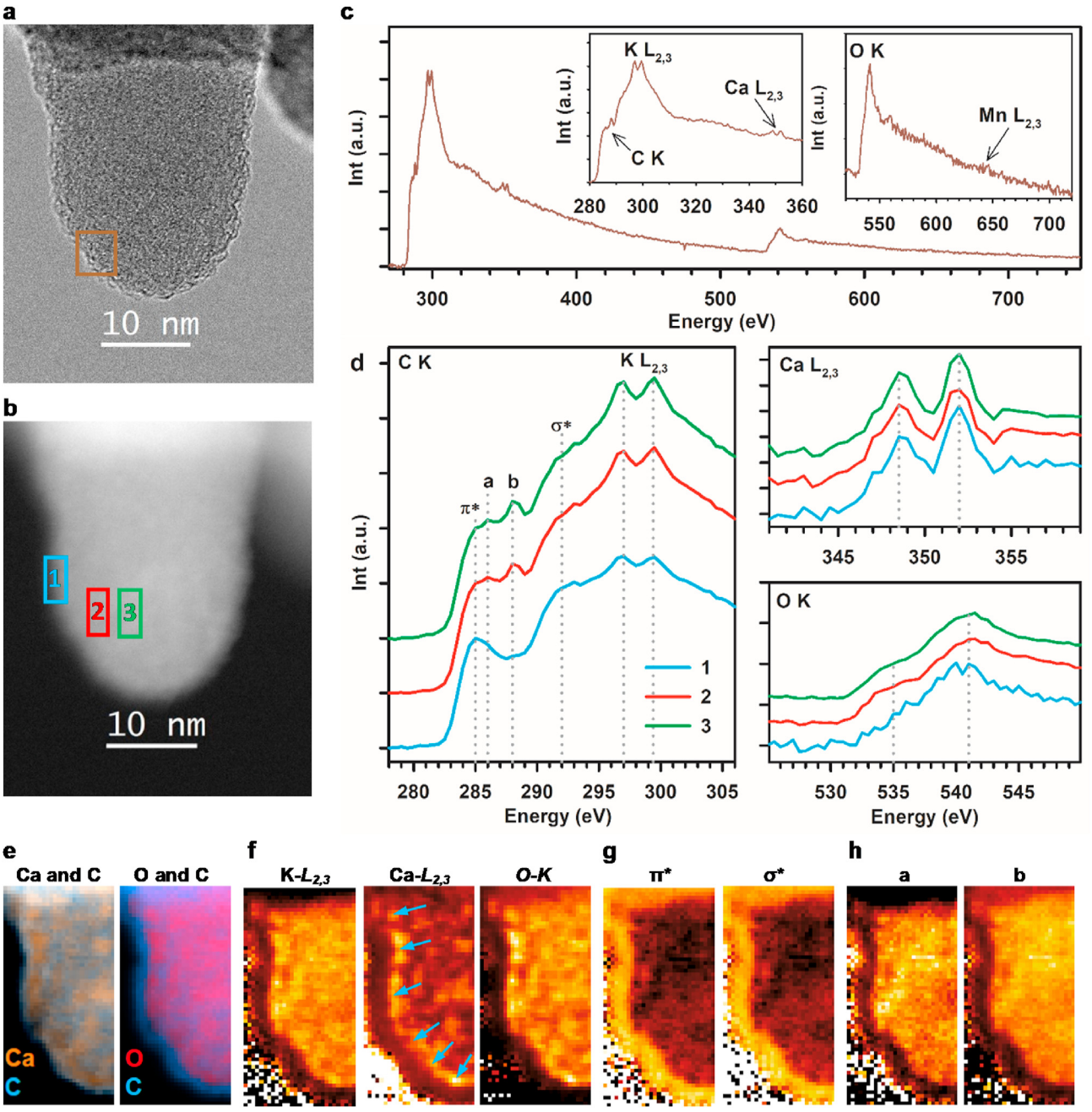

Fig. 4. STEM-EELS analysis of non-spherical soot particles. (**a**) BF-STEM image. (**b**) HAADF-STEM image. (**c**) Overview EELS signal from the areas marked in **a** showing the carbon *K* edge (285 eV), potassium $L_{2,3}$ edges (296 eV, 294 eV), calcium $L_{2,3}$ edges (350 eV, 346 eV), oxygen K edge (532 eV), and possibly also the manganese $L_{2,3}$ edges (651 eV, 640 eV). (**e**) Composite EELS maps of the left side of the particle showing the calcium and carbon content and the oxygen and carbon content, respectively. (**f**) Ratio maps of heteroatom content, potassium, calcium, and oxygen. (**g-h**) Ratio maps of carbon compounds, (**g**) contribution from graphitic π* and σ* bonds and (**h**) contribution from the non-graphitic bonds, i.e. ketone bonds (peak a maps) and carboxyl bonds (peak b maps). The reactor temperature was 1313 °C. Additional STEM-EELS analysis of a similar non-spherical soot particle can also be found in Fig. S8. Ratio maps are displayed on a false color scale to enhance legibility, color in order of increasing intensity: black, red, yellow, and white. Beyond the particle edge (in vacuum) the ratio-map contrast is not meaningful, pixels values are NaN. (A colour version of this figure can be viewed online.)

carbonates [86,88] supporting the peak assignment made for peak a and c in the carbon *K*-edge. ELNES of the manganese $L_{2,3}$ edge is presented in Fig. S9. Although the signal was noisy, it was possible to identify a major peak at 645 eV from the central part of the particle, indicating the presence of manganese in the sample and confirming the results seen in the overall EELS signal (see Fig. 4c).

Composite maps of calcium and carbon, and oxygen and carbon (Fig. 4e, and Fig. S8e) showed that the particle had a stratified structure and that in general there was a co-location of calcium and oxygen. The corresponding individual elemental EELS maps of carbon, oxygen and calcium used to create the results in Fig. 4e can be found in Fig. S11. In order visualize the relative distributions of heteroatoms (i.e. K, Ca, and O), graphitic bonds (π* and σ* peaks), and non-graphitic bonds (a, b, and c peaks) in the particle, so-called ratio maps where created by normalizing the data to the intensity of the carbon K edge (for details, see Section 2). Ratio maps are the preferable visualization technique if there are overlapping peaks in the EELS signal - as in the current case. The ratio maps of the heteroatoms, graphitic and non-graphitic peaks are presented Fig. 4f–h and Figs. S8f-h. The ratio maps for the heteroatoms show

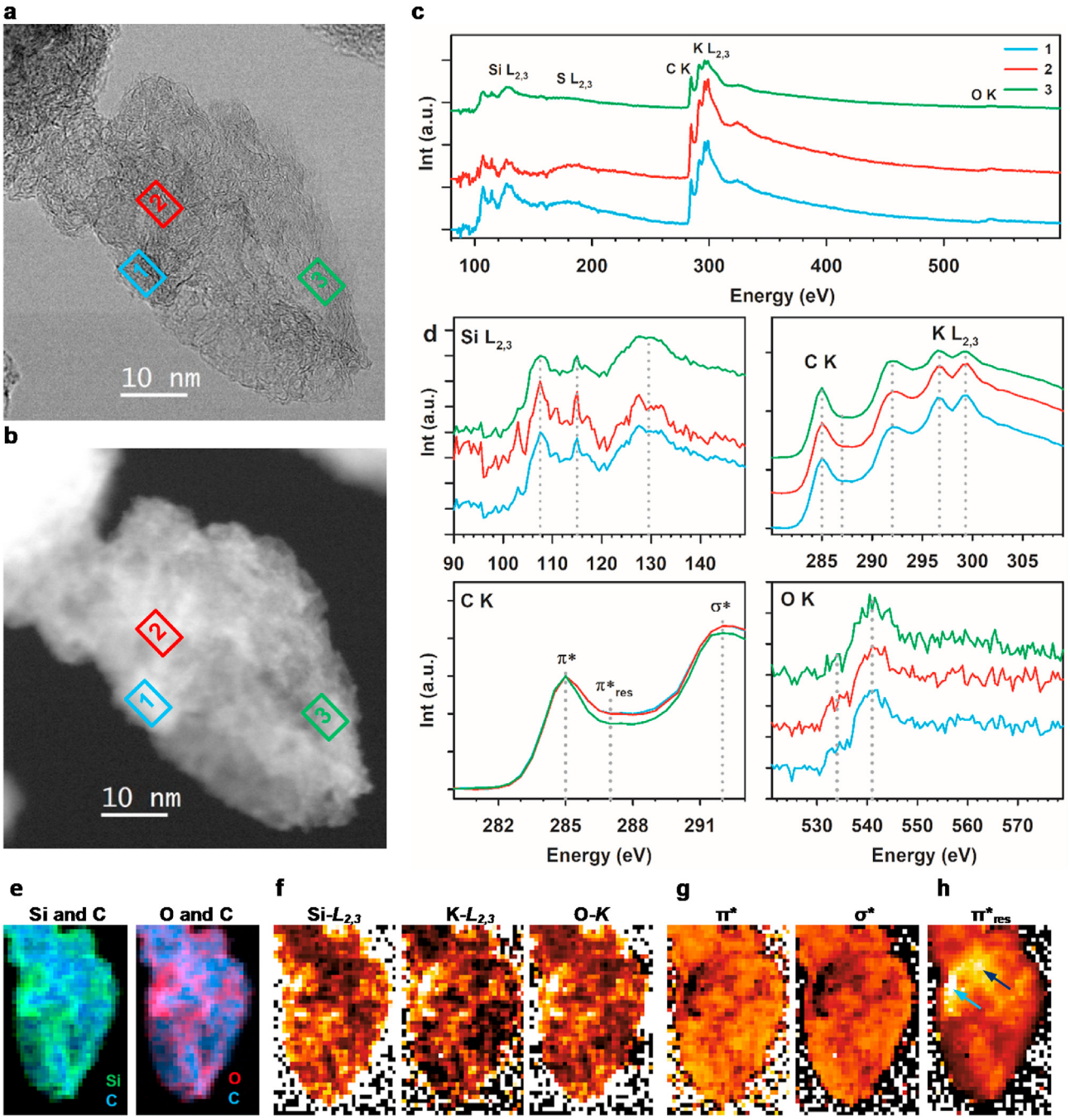

Fig. 5. STEM-EELS analysis of highly oxidized soot particles. **(a)** BF-STEM image. **(b)** HAADF-STEM image. **(c)** Overview EELS signal extracted from the areas marked in **a** and **b** showing the silicon $L_{2,3}$ edge (99 eV), carbon *K* edge (285 eV), potassium $L_{2,3}$ edges (296 eV, 294 eV), oxygen *K* edge (532 eV) and possible also the sulfur $L_{2,3}$ edge (165 eV). **(d)** ELNES of the silicon $L_{2,3}$ edge, carbon *K* edge and potassium $L_{2,3}$ edge, zoomed in area of the carbon *K* edge showing the π* and σ* peak and finally the oxygen *K* edge. The location of the residual peak (π^*_{res}) at 287 eV identified in the Gaussian fitting routines (see Fig. S12) are also shown in the figure. The ELNES signals in plate **d** were extracted from the areas marked in **a** and **b**. **(e)** Composite EELS maps of the particle, silicon and carbon and oxygen and carbon **(f)** Ratio maps of heteroatom content, silicon, potassium, and oxygen. **(g-h)** Ratio maps of carbon compounds, **(g)** contribution from graphitic π* and σ* bonds and **(h)** the π^*_{res} peak map which shows the distribution non-graphitic carbon bonds when the relative intensities of the π^*_{res} map differs significantly from that of the π* map. The reactor temperature was 1430 °C. Ratio maps are displayed on a false color scale to enhance legibility, color in order of increasing intensity: black, red, yellow, and white. Beyond the particle edge (in vacuum) the ratio-map contrast is not meaningful, pixels values are NaN. (A colour version of this figure can be viewed online.)

that compared to calcium and oxygen, potassium was slightly more homogeneously distributed within the particle (see Fig. 4f and Fig. S8f). Furthermore, the particle had a graphitic structure close to the edge and a non-graphitic structure in the interior of the particle (see Fig. 4g–h; Figs S8g and S8h). The good agreement between relative intensities of the π* and σ* ratio maps (see Fig. 4g and Fig S8g) also rules out any major orientation effects that could affect the interpretation of the graphitic content of the particle. The overall positive correlation between the presence of heteroatoms and non-graphitic bonding throughout the whole particle (see Fig. 4f–h; Figs S8f and S8h) was a strong indication that peaks a, b and c were indeed due to carbon-oxygen bonding environments, with carbon-oxygen functional groups locally disrupting the graphitic network. Between the graphitic edge and the non-

graphitic interior, there was also a very thin layer (indicated by blue arrows in Fig. 4f and S8f), where both the heteroatom content, (especially calcium and oxygen) and the non-graphitic contribution from ketone bonds (a peak) and carboxyl bonds (b peak) were, for the most part, significantly higher compared to the rest of the particle (most clearly seen fig. S8f-h). The local change in chemistry in this thin "border region" might be indicative of a reaction zone in the particle.

3.3. Highly oxidized soot particles

Fig. 5 shows the STEM-EELS results for an oxidized soot particle. From the fringe pattern seen in the BF-STEM image (Fig. 5a), it was still possible to identify regions wherein the graphitic structure of the particle was preserved. In the HAADF-STEM image (Fig. 5b), these regions had higher intensity, indicating a denser and/or thicker material. A higher density could be explained by selective oxidation; i.e., more carbon was converted in the thinner regions of the particle. From the overall EELS signal presented in Fig. 5c, it was possible to detect silicon, carbon, potassium, oxygen and traces of sulfur in the particle.

The ELNES of the silicon $L_{2,3}$ edge, carbon *K* edge, potassium $L_{2,3}$ edge, and the oxygen *K* edge extracted from three different regions of the particle are shown in Fig. 5d. As for spherical soot particles, the ELNES of the silicon $L_{2,3}$ edge was consistent with SiO_2, with an onset at ~104 eV, two major peaks at ~107 eV and ~114.5 eV, and a broader peak centered at ~129 eV. All spectra indicated that the particle was mainly graphitic (i.e. predominantly sp^2 bonded), evidenced by the carbon *K* edge exhibiting graphitic π* and σ* peaks at ~285 eV and 292 eV, respectively. However, the Gaussian peak fitting routine (see Fig. S12) also indicated that there was a residual contribution from non-graphitic bonding with a peak located at ~287 eV, marked π*res in the figure. Superimposed on the carbon *K* σ* peak, the potassium $L_{2,3}$ edge was clearly resolved: the signal from potassium relative to carbon was higher in the first and second regions than in the third region, implying corresponding changes in elemental concentration. The oxygen *K* edge was noisy, with a major peak at ~540 eV and a possible pre-peak at ~534 eV in the spectra sampled at the first and second regions.

Composite EELS maps of carbon-oxygen and carbon-silicon (see Fig. 5e) showed a stratified distribution of elements in the particle. The elemental maps of carbon, oxygen and silicon used to generate the results shown in Fig. 5e are shown in Fig. S13. Compared to the spherical soot particles, silicon and oxygen were not only confined to a thin continuous surface layer; the composite maps were consistent with silicon and oxygen being present within the particle. A spectrum demonstrating the Gaussian fitting routine used for EELS data is shown in Fig. S12. The resulting ratio maps (Fig. 5f–h) of the heteroatoms (Si, K, and O), graphitic (π* and σ*) and non-graphitic (π^*_{res}) bonding showed that, in general, there was co-location between the heteroatoms and non-graphitic carbon compounds; the contribution from graphitic compounds (π* and σ*) in many of these regions was reduced. Also, for this particle, there was a good correspondence between the π* and σ* ratio maps (see Fig. 5g) indicating that the orientation effects that could affect the results are limited.

The presence of heteroatoms clearly affected the carbon structure here, however, likely to a lesser degree and/or for lower concentrations than for non-spherical soot particles since no distinct peaks were observed in the carbon *K* edge ELNES between the graphitic π* and σ* peaks (see Fig. 5d). Intensity changes in the π^*_{res} peak ratio map, differing from that of the π* and σ* maps, can probably be attributed to carbon-oxygen bonding and/or "fullerenic" non-planar sp^2 carbon bonding. The latter has previously been observed in the heat treatment procedure of phenolic resin-based carbon which, after heat treatment, developed a micro-porous nanostructure [59] similar to those observed here in BF-STEM images (Fig. 5a) or in HRTEM images [36] of the highly oxidized soot particles. Furthermore, a micro-porous nanostructure with highly curved graphene sheets has also been observed to be formed in in-situ HRTEM soot oxidation studies [68]. Based on the ratio maps, we can tentatively associate local increases in π^*_{res} ratio map intensity with local changes in bonding: an increase in π^*_{res} ratio map intensity accompanied by an increase in heteroatom ratio map intensities and a decrease in π* ratio map intensity appears to be indicative of carbon-oxygen bonding (see in particular the "arc-shaped" region in the middle-left of the particle, location exemplified with a blue arrow in Fig. 5h). In contrast, an increase in π^*_{res} ratio map intensity accompanied by a decrease in heteroatom and π* ratio map intensities was consistent with fullerenic bonding (see in particular the center top-half of the particle, location exemplified with a black arrow in Fig. 5h).

3.4. Carbon-inorganic fused agglomerates

A part of a carbon-inorganic fused agglomerate studied by STEM-EELS is shown in Fig. 6. No crystalline fringes were seen in the BF-STEM image (Fig. 6a) and the HAADF-STEM image (Fig. 6b) intensity was suggestive of a large density and/or thickness variation within the particle. EEL spectra showed the presence of phosphorous, sulfur, carbon, potassium, calcium and oxygen in all four sampling locations (Fig. 6c), however, no silicon was detected in this particle.

The ELNES of the phosphorous $L_{2,3}$, sulfur $L_{2,3}$, carbon *K*, potassium $L_{2,3}$, calcium $L_{2,3}$ and the oxygen *K* edges are presented in Fig. 6c and d. The phosphorous $L_{2,3}$ edge was characterized by two major peaks at ~139 eV and at ~147 eV. The most likely phosphorous compounds here were $Ca_3(PO_4)_2$ and/or $Ca_2P_2O_7$ – and the ELNES shows similarities with phosphorous $L_{2,3}$ edge XANES of these two compounds [89]. Furthermore, $Ca_3(PO_4)_2$ has previously been predicted as a thermodynamically stable compound in carbon-inorganic fused agglomerates [36]. The ELNES of the carbon *K* edge showed similarities with the spectra from the non-spherical soot particle (see Fig. 4d) and the spectra extracted from areas 2 and 4 exhibit strong π* (~285 eV) and σ* (~292 eV) peaks, associated with graphitic carbon. Two additional peaks were found between the π* peak and the σ* peak, at ~286.5 eV and ~290 eV, marked a and c in the figure, indicating that non-graphitic carbon bonding was present in the particle. Furthermore, it was possible to approximate the shape of the ELNES signal using Gaussian peak least-squares fitting as described in the methods section, including the aforementioned "a", "c", π* and σ* peaks, see Fig S14. For the spectra extracted from regions 1 and 3, the π* peak at ~285 eV was significantly reduced and, instead, the two previous minor peaks at ~286.5 eV and ~290 eV became dominant. As for the non-spherical soot particle, these extra peaks can probably be attributed to a carbon-oxygen bonding environment. The minor peak at ~286.5 eV is probably a result of carbonyl bonds. The major peak at ~289 eV was consistent with that of the carbonate structure and judging from the high calcium signal, the presence of some form of $CaCO_3$ compounds was likely, perhaps in a solid solution compounds with phosphorous and potassium since these elements were also present in the same area of the particle. Different forms of K–Ca-carbonates, i.e. $K_2Ca_2(CO_3)_3$ and $K_2Ca(CO_3)_2$, and accompanying carbonate and phosphate phases in the form of carbonate apatite, $Ca_{9.9}(PO_4)_6(CO_3)_{0.9}$ have recently been identified by XRD in ash produced from char combustion of silicon-poor woody biomass [90] showing that these type compounds can be formed in similar processes. The calcium $L_{2,3}$ and the oxygen *K* edge ELNES showed only the major peaks without any significant pre-peaks that could

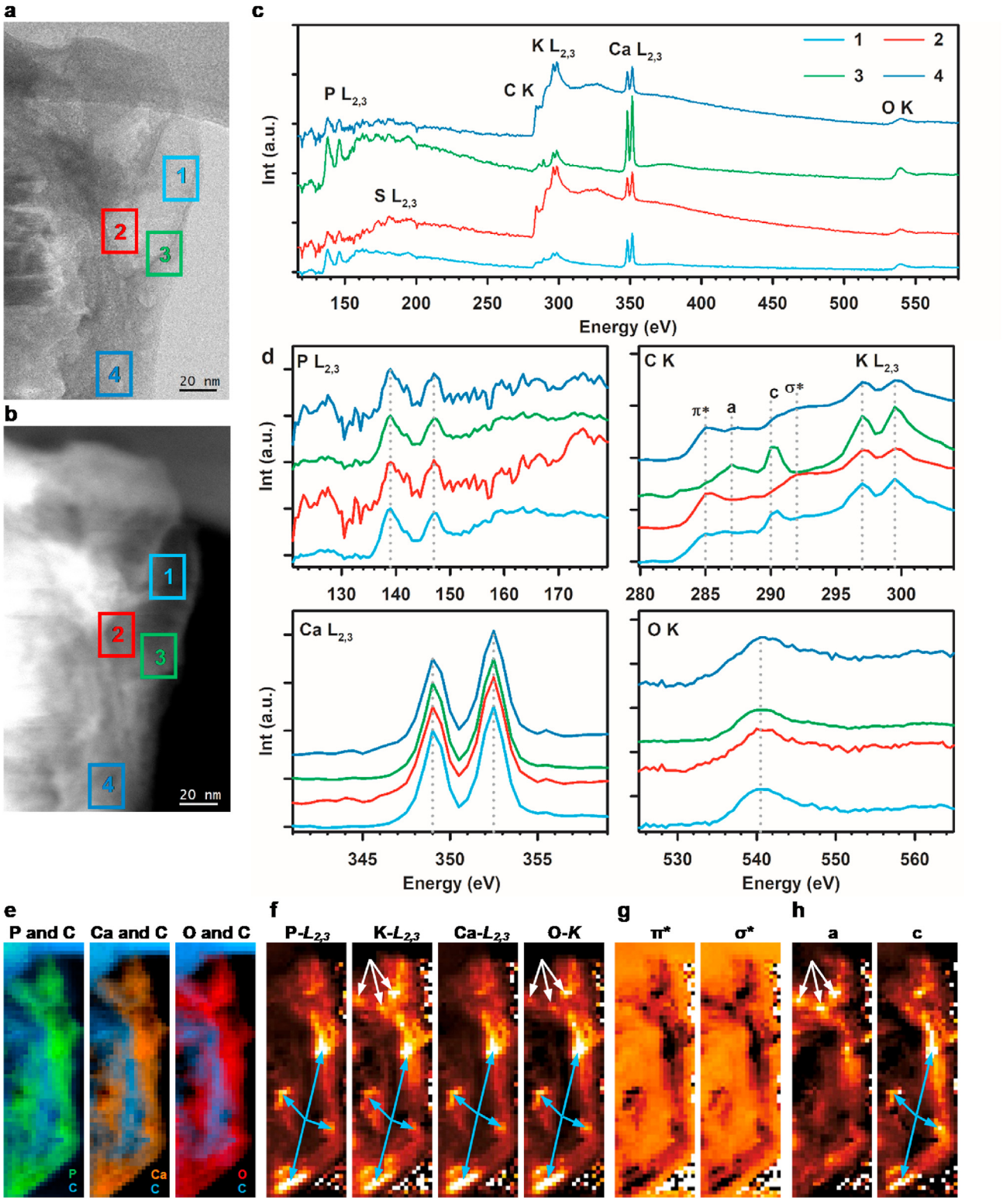

Fig. 6. STEM-EELS analysis of carbon – inorganic fused agglomerate (a) BF-STEM image. **(b)** HAADF-STEM image. **(c)** Overview EELS signal extracted from the areas marked in **a** and **b** showing the phosphorous $L_{2,3}$ edge (132 eV), sulfur $L_{2,3}$ edge (165 eV), carbon *K* edge (285 eV), potassium $L_{2,3}$ edges (296 eV, 294 eV), calcium $L_{2,3}$ edges (350 eV, 346 eV), and oxygen *K* edge (532 eV). **(d)** ELNES of the phosphorous $L_{2,3}$ edge, carbon *K* edge and potassium $L_{2,3}$ edge, calcium $L_{2,3}$ edge, and finally the oxygen *K* edge. **(e)** Composite EELS map of the particle, phosphorous and carbon, calcium and carbon, oxygen and carbon. **(f)** Ratio maps of heteroatom content, phosphorous, potassium, calcium and oxygen. **(g-h)** Ratio maps of carbon compounds, **(g)** contribution from graphitic compounds (π* and σ* peak maps) and **(h)** contribution from the non-graphitic compounds, i.e. ketone bonds (peak a maps) and carbonate bonds (peak c maps). The reactor temperature was 1550 °C. Ratio maps are displayed on a false color scale to enhance legibility, color in order of increasing intensity: black, red, yellow, and white. Beyond the particle edge (in vacuum) the ratio-map contrast is not meaningful, pixels values are NaN. (A colour version of this figure can be viewed online.)

be helpful in the identification of the possible chemical compounds.

The composite EELS map showed a stratified elemental distribution in the particle (Fig. 6e). The corresponding elemental EELS maps of phosphorous, carbon, calcium and oxygen that were used to generate results shown in Fig. 6 are shown in Fig. S15. Phosphorous, calcium and oxygen were, in general, enriched in the same locations, i.e., at the right edge of the particle and in the interior. Between these two regions, carbon-rich lamellar material was seen. From the ratio maps of the heteroatoms (Fig. 6f), the graphitic compounds (Fig. 6g) and non-graphitic contribution (Fig. 6h) there was, in general, a positive correlation between the heteroatoms and the non-graphitic compounds (ketone bonds (a peak map) and carbonate bonds (c peak maps) and a negative correlation to the graphitic compounds (peak π* and σ* maps), clearly showing that the inorganic elements affected the carbon structure in large parts of the particle. In small areas of the particle, there was also a difference in the distribution of the non-graphitic compounds that indicated heterogeneous chemistry within the non-graphitic regions. A high ketone signal (a-peak maps) corresponds to a high potassium and oxygen signals (exemplified with white arrows in Fig. 6f and h) whereas a high carbonate signal (c-peak maps) corresponds to high phosphorous, potassium, calcium and oxygen signals (exemplified with blue arrows in Fig. 6f and h). The first observation indicates that potassium and oxygen started to react with the graphitic carbon structure forming the first carbon-oxygen bond (i.e. the ketone bond) in the reaction scheme towards the thermodynamic stable carbonate bonding environment. The second observation indicates the simultaneous presence of K–Ca-carbonate and Ca-carbonate-phosphates and thereby that the oxidation process was finished in these areas of the particle due to the formation of the thermodynamically stable carbonate bond.

3.5. Nanostructure-elemental composition relationships

The objective of the joint analysis of nanostructure and EELS data was to uncover relationships between these in soot and to provide further hints on possible particle formation mechanisms. The available micrographs were processed to extract interlayer spacing, fringe length, fringe tortuosity, and symmetry parameters. After the registration of STEM images and EELS maps, it was possible to study relationships between nanostructure and elemental composition on a pixel-by-pixel basis in the case of interlayer spacing and symmetry, and on fringe-by-fringe basis in the case of fringe length and fringe tortuosity. In other words, joint data for structural parameters and heteroatom concentration were available. Due to the abundance of extracted structural data [63,64], pixel-level image analysis allowed for the discovery of even weak correlations and trends. Given this, an important objective was to elaborate on the relationship between silicon content (in the form of mostly SiO_2, as discussed in Sections 3.1 and 3.3) and nanostructure in particles that contained silicon in the surface layer.

Fig. 7 shows results from the joint structure-elemental composition analysis. Only STEM images of soot particles were processed, since these contained visible fringes that corresponded to projections of carbon lamellae that satisfied the Bragg condition; data from carbon-inorganic fused aggregates were not analyzed. For these particles, namely, spherical soot and oxidized soot (EELS analyses shown in Figs. 3 and 5, respectively), the only heteroelement originating from the fuel ash found in detectable quantities in both data sets was silicon; therefore, we present correlations between nanostructure and the relative amount of silicon. Structural analysis was done in image areas that were segmented based on the amount of silicon (as determined by EELS): areas of high and low silicon concentration were defined, and results are presented for these regions separately. This was carried out for both spherical soot and oxidized soot particles. In general, regions of low and high silicon content were defined by thresholding the EELS Si maps: rescaling to [0, 1] and setting a threshold of 0.5 to separate regions of low (below 0.5) and high (above 0.5) relative Si concentration. The results are shown in Fig. 7.

For the spherical soot sample, a noticeable trend can be observed: the nanostructure of high-silicon regions appeared more ordered than that of the low-silicon regions in the sense that in high-silicon regions, fringes were longer and less curved; nematic symmetry was stronger, polar symmetry was weaker and d_{002} was significantly closer to that of graphite than in regions of low silicon content. Naively, this indicates that the presence of silicon correlates with a more compact, ordered, graphitic structure. This is counterintuitive, as the presence of both substitutional and interstitial heteroatoms is expected to increase the interlayer spacing and fringe curvature due to increased ring strain, subsequently lowering nematic symmetry. To explain this, we note that for spherical soot particles, silicon appeared to be exclusively present on the surface, indicating that the dominant mechanism for capturing silicon was adsorption after the soot was incepted and a primary particle formed. Consequently, in the inner amorphous core silicon was not detected – this is the region where interlayer spacing was high, due to the less ordered nature of the core. Thus, the high partitioning of silicon between the graphitic particle shell and amorphous core alone could cause the trends seen in Fig. 7a–e. To correct for this, non-graphitic regions with weak nematic symmetry were filtered out, and the relationship between d_{002} and the amount of silicon was studied only within the more graphitic regions near the edge. As such, the effect of the fractioning of silicon between the surface and the core, and the coincidental fact that the structure close to the surface was graphitic, were decoupled in the analysis. A linear model in the form of $d_{002} = a + b \times C_{Si}$, where C_{Si} is the relative amount of silicon, was robustly fit to the data.

The result of this linear analysis is shown in Fig. 7f; as seen, the slope of the fit indicated that the more silicon was present the larger the separation was between carbon lamellae – this is more consistent with intuition. The coefficient of determination (R^2) was low, approximately 0.1; however, standard errors of parameters a and b, corresponding p-values and the F-statistic all implied that the observed trend was significant, however weak. We note that a linear model did not appear to be an optimal choice for the data: the relationship appeared to be nonlinear, as d_{002} values increased almost asymptotically at approximately 80% relative silicon content. Nevertheless, the linear analysis was sufficient to uncover the positive correlation between silicon content and interlayer spacing. In the case of oxidized soot, possibly because the absolute amount and relative variation of the amount of silicon was higher than in spherical soot, bulk analysis already revealed the direct proportionality between d_{002} and the amount of silicon. In other words, the presence of silicon was accompanied by an increase in d_{002} in this sample. This effect was found to be weak: this might be related to that only trace amounts of silicon were adsorbed on the particle surface.

Trends seen in the joint nematic symmetry-silicon content data were similar: in both spherical soot and oxidized soot, high-silicon regions exhibited higher nematic symmetry than regions of low silicon. Altogether, these observations suggest that the silicon present in spherical and oxidized soot was captured after primary particles had formed, via adsorption to the surface. After oxidation and the conversion of reactive particle cores, silicon-rich outer shells collapsed and formed the “crumpled shell” structure that was observed in in-situ oxidation studies of pure soot [68]. This explains the seemingly contiguous “islands” of high-silicon areas, e.g., as seen in Fig. S2b.

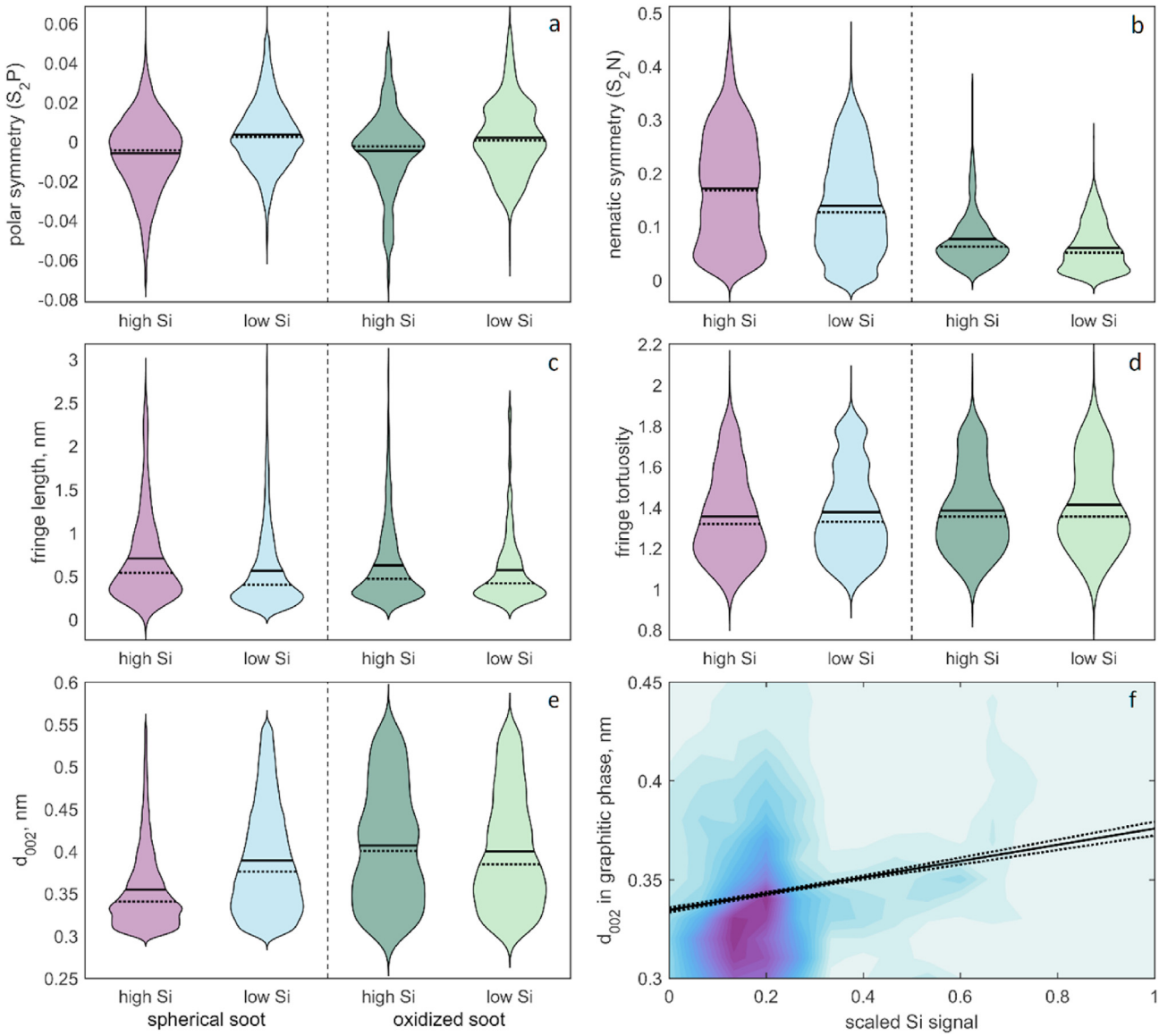

Fig. 7. Results from joint quantitative analysis of nanostructure and elemental composition, namely, the amount of silicon. The first five plots show distributions of various structural parameters grouped by silicon-content. The distributions of two samples, spherical soot and oxidized soot, are shown in purple-blue and green hues, respectively. Plots in **(a)**–**(e)** only differ in the structural parameter that is visualized: **(a)** nematic symmetry (S_2N) at a scale of 7 nm **(b)** polar symmetry (S_2P) at a scale of 25 nm **(c)** fringe length **(d)** fringe tortuosity **(e)** interlayer spacing (d_{002}). Solid lines indicate the sample mean, while dotted lines indicate the sample median. **(f)** Correlation between d_{002} and the relative amount of silicon in graphitic regions within spherical soot particles. Instead of plotting data points individually, a kernel density estimate of the bivariate probability density distribution is shown. Hues of blue from light to dark indicate probability density from low to high, respectively. The solid line shows a linear fit over the data. Dotted lines show the confidence bound on the linear fit. (A colour version of this figure can be viewed online.)

3.6. New insights into particle formation

A detailed description of the overall particle formation mechanism for soot/carbon-rich nanoparticles at high temperature, and in a reducing atmosphere that contains gaseous ash-forming elements (i.e., entrained flow gasification of wood powder) has been proposed elsewhere [36] and therefore we only comment on the new insights provided by the aberration corrected STEM-EELS investigation here. Independent of reactor conditions, a small portion of the silicon from the fuel vaporized, and a part finally adsorbed on, and diffused into the turbostratic graphene planes at the surface of the soot particle – this silicon was detected alongside oxygen, in large parts as SiO_x (mixture of elemental Si and SiO_2). Silicon only appearing as a surface layer implied that soot particles formed first and gaseous silicon or silicon compounds (e.g. SiO or SiO_2) adsorbed on these later. If the silicon enters the soot structure as reduced compounds, oxidation to SiO_2 can proceed mainly through reactions with O_2, CO_2 or H_2O. Subsequently, since oxidation was faster at neck-sites, the relative concentration of SiO_2 was highest in the necks as well.

According to thermodynamics, potassium fed with the fuel is in the gas phase at process temperatures above 1000 °C [36], and therefore can interact with carbon during soot formation. Earlier HRTEM-EDS analyses have shown that spherical soot particles have traces of potassium [36] and most likely the potassium is homogeneously incorporated into the soot structure since (i) no distinct layer of potassium was observed in the STEM-EELS of spherical soot particles, and (ii) the distribution of potassium was relatively homogeneous (in the case of non-spherical and highly oxidized particles). As the oxidation of soot progresses, potassium and SiO_2 can

react, forming low-temperature silicate melts that wet the graphite and enter micro-pores formed during burning. The graphitic structure of the carbon was relatively unaffected by the presence of a silicate melt. However, if some π^*_{res} peak ratio map intensity changes in Fig. 5 can indeed be attributed to a carbon-oxygen bonding environment and not just to a fullerenic carbon structure formed during oxidation of the particle, this would be consistent with the silicate melt dissolving and reacting with at least a part of the graphitic carbon. Based on the tentative comparative analysis of the ratio maps in Fig. 5 (see section 3.3), this appears to be a likely scenario.

The non-spherical soot particles may have undergone a different formation mechanism than the spherical soot particles. The presence of calcium relatively evenly distributed in the particle indicates that these particles were formed under very high temperature in an environment with a high concentration of inorganics (i.e., calcium and potassium), as both elements were detected in EEL spectra. Major amounts of gas-phase calcium, i.e., Ca(g), CaOH(g), and $Ca(OH)_2$(g), have been predicted at process temperatures above 1400 °C [36]. Interestingly, the carbon structure was also different in the spherical soot particles and their differing inorganic composition affected the carbon formation process, leading to high temperature oxygen functionalization of the graphitic carbon structure. At the highest temperatures (>2000 °C) that occurred at high oxygen-to-fuel ratios, phosphorous can also be volatilized as PO(g) and PO_2(g) [36]. In general, phosphorous is the most reactive negative anion in thermochemical conversion of biomass [91], and different K–Ca-phosphates are thermodynamically stable in this environment, suppressing K–Ca-silicate formation [36]. The chemistry leading to the formation of the carbon-inorganic fused agglomerate is likely very complicated and initially involves graphitic carbon from the soot and an inorganic melt. Thereafter, carbon-oxygen functional groups (e.g. ketone, carboxyl) form as intermediates in the graphite-inorganics reaction, before finally forming the more thermodynamically stable carbonate bond, in some kind of a high temperature mineralization process. Inorganic elements, especially calcium (and phosphorous when it is present in the particle), may play an important role here, since the significant carbon-oxygen bonding environment (especially carbonate bonds) were only detected when calcium was present in the sample. Furthermore, without the presence of inorganic elements that can form high temperature stable condensed phases as a result of the oxidation process, the carbon atoms will simply be released from the graphite structure to the gas phase as CO and/or CO_2.

3.7. EELS vs synchrotron X-ray absorption analysis of soot particles

In past studies of soot particles, it was suggested that (S)TEM-EELS used to lack the resolution or sensitivity to detect spectral features at the carbon *K* edge associated with local variations in functional chemistry, as compared to the more widely-used synchrotron-based X-ray absorption spectroscopy [75]. Our results clearly demonstrate that the current generation of STEM instruments can resolve changes in carbon bonding within soot particles in this energy range (285–292 eV), with nanometer spatial resolution.

In the present work, we focused on the simultaneous acquisition of core loss ionization edges from a range of elements while still maintaining an energy resolution high enough for a careful analysis of the fine structure of these edges. Although the mode of operation necessary for these measurements dictates a moderate energy resolution (limited in practice by the point-spread-function of the detector and the energy dispersion used), it was still possible to resolve fine structures changes in the carbon *K* ionization edge that we could associate with changes in carbon bonding at the nanoscale.

A much higher energy resolution, comparable to or better than that of X-ray absorption spectroscopy [75], is now available in state-of-the-art monochromated STEM-EELS systems [92] that maintain atomic spatial resolution [93,94]. Further work will focus on using monochromated STEM-EELS to study the ELNES of the carbon K edge (and other ionization loss edges of interest) from soot and related materials could be investigated at a level of detail rivalling that of X-ray absorption spectroscopy, with the added benefit of nanometer-to-atomic spatial resolution [79,95]. By combining this with simultaneous elemental mapping, STEM-EELS allows for finding correlations between the distributions of heteroatoms and different types of carbon bonding within individual soot particles which helps us explore and understand the nano-chemistry of soot.

4. Conclusions

In this work, we demonstrated that aberration-corrected STEM-EELS can be used to study metal-containing, paracrystalline soot with a three-dimensional nanostructure. Spatially resolved elemental mapping together with information on the predominant chemical compounds were achieved at nanometer spatial resolution. Using this technique, we showed that all spherical soot particles were coated by a silicon- and oxygen rich layer and that calcium likely affected the graphitic structure of non-spherical soot and carbon-inorganic fused agglomerates. In addition, we demonstrated the first joint quantitative analysis of nanoscale carbon structure and elemental distribution in soot. These results revealed a positive correlation between silicon content and interlayer spacing in soot, hinting that silicon in the form of SiO_2 might have a distorting effect on the carbon nanostructure. The detailed information provided by aberration-corrected STEM-EELS can be used to better understand the complex formation mechanism of metal-containing soot particles. Results and insights enabled by the approach demonstrated here can potentially help inform the choice of additives or aid in the design of fuel blends that minimize the formation of similar, hybrid particles in combustion or gasification systems.

CRediT authorship contribution statement

Henrik Wiinikka: Conceptualization, Formal analysis, Writing - original draft, Project administration, Funding acquisition. **Fredrik S. Hage:** Methodology, Formal analysis, Investigation, Data curation, Writing - review & editing, Visualization. **Quentin M. Ramasse:** Methodology, Formal analysis, Writing - review & editing, Funding acquisition. **Pal Toth:** Methodology, Software, Formal analysis, Writing - original draft, Writing - review & editing, Visualization.

Declaration of competing interest

The authors declare that they have no known competing financial interests or personal relationships that could have appeared to influence the work reported in this paper.

Acknowledgements

The Bio4Energy, a strategic research environment appointed by the Swedish government and the Swedish Center for Gasification financed by the Swedish Energy Agency and member companies are acknowledge for founding of this work. The SuperSTEM Laboratory is the U.K. National Research Facility for Advanced Electron Microscopy, supported by the Engineering and Physical Sciences

Research Council (EPSRC). The authors thank Orsolya Lukacs for her assistance in preparing artwork.

Appendix A. Supplementary data

Supplementary data to this article can be found online at https://doi.org/10.1016/j.carbon.2020.12.004.

References

[1] J.S. Lighty, J.M. Veranth, A.F. Sarofim, Combustion aerosols: factors governing their size and composition and implications to human health, J. Air Waste Manag. Assoc. 50 (2000) 1565–1618.
[2] K. Qin, P.A. Jensen, W. Lin, A.D. Jensen, Biomass gasification behavior in an entrained flow reactor: gas product distribution and soot formation, Energy Fuels 26 (2012) 5992–6002.
[3] Z. Wang, Y. Qi, H. Liu, Y. Long, J.X. Wang, Experimental study on pre-ignition and super-knock in gasoline engine combustion with carbon particle at elevated temperatures and pressures, 2015. SAE Technical Paper 2015-01-0752.
[4] B. Booth, N. Bellouin, Climate change: black carbon and atmospheric feedbacks, Nature 519 (2015) 167.
[5] Z. Klimont, K. Kupiainen, C. Heyes, P. Purohit, J. Cofala, P. Rafaj, et al., Global anthropogenic emissions of particulate matter including black carbon, Atmos. Chem. Phys. 17 (2017) 8681–8723.
[6] N.L. Mills, H. Törnqvist, M.C. Gonzalez, E. Vink, S.D. Robinson, S. Söderberg, et al., Ischemic and thrombotic effects of dilute diesel-exhaust inhalation in men with coronary heart disease, N. Engl. J. Med. 357 (2007) 1075–1082.
[7] M.Z. Jacobson, Strong radiative heating due to the mixing state of black carbon in atmospheric aerosols, Nature 409 (2001) 695–697.
[8] J.B. Donnet, Carbon Black: Science and Technology, CRC Press, 1993.
[9] Carbon Black – A global market overview, http://industry-experts.com/verticals/chemicals-and-materials/carbon-black-a-global-market-overview. Accessed 2019-03-27.
[10] K.O. Johansson, M.P. Head-Gordon, P.E. Schrader, K.R. Wilson, Michelsen Ha, Resonance-stabilized hydrocarbon-radical chain reactions may explain soot inception and growth, Science 361 (2018) 997–1000.
[11] M.R. Kholghy, A. Veshkini, M.J. Thomson, The core-shell internal nanostructure of soot - a criterion to model soot maturity, Carbon 100 (2016) 508–536.
[12] R.L. Vander Wal, A.J. Tomasek, Soot oxidation: dependence upon initial nanostructure, Combust. Flame 134 (2003) 1–9.
[13] R.L. Vander Wal, A.J. Tomasek, Soot nanostructure: dependence upon synthesis conditions, Combust. Flame 136 (2004) 129–140.
[14] M.P. Ruiz, R.G. de Villoria, A. Millera, Alzueta Mu, R. Bilbao, Influence of the temperature on the properties of the soot formed from C_2H_2 pyrolysis, Chem. Eng. J. 127 (2007) 1–9.
[15] I.C. Jaramillo, C.K. Gaddam, R.L. Vander Wal, C.H. Huang, J.D. Levinthal, J.S. Lighty, Soot oxidation kinetics under pressurized conditions, Combust. Flame 161 (2014) 2951–2965.
[16] M.R. Muley, A. Chauhan, S. Patel, V. Balakrishnan, A. Halder, R. Vaish, Candle soot: journey from pollutant to functional material, Carbon 144 (2019) 684–712.
[17] S. Khodabakhshi, P.F. Fulvio, W. Andreoli, Carbon black reborn: structure and chemistry for renewable energy harnessing, Carbon 162 (2020) 604–649.
[18] J.C. Corbin, A.A. Mensah, S.M. Pieber, J. Orasche, B. Michalke, M. Zanatta, et al., Trace metals in soot and $PM_{2.5}$ from heavy-fuel-oil combustion in a marine engine, Environ. Sci. Technol. 52 (2018) 6714–6722.
[19] J.C. Hower, U.M. Graham, A. Dozier, M.T. Tseng, R.A. Khatri, Association of the sites of heavy metals with nanoscale carbon in a Kentucky electrostatic precipitator fly ash, Environ. Sci. Technol. 42 (2008) 8471–8477.
[20] V. Kurian, R. Gupta, Distribution of vanadium, nickel, and other trace metals in soot and char from asphaltene pyrolysis and gasification, Energy Fuels 30 (2016) 1605–1615.
[21] L. Liu, S. Kong, Y. Zhang, Y. Wang, L. Xu, Q. Yan, et al., Morphology, composition, and mixing state of primary particles from combustion sources - crop residue, wood, and solid waste, Sci. Rep. 7 (2017) 5047.
[22] J. Moldanová, E. Fridell, H. Winnes, S. Holmin-Fridell, J. Boman, A. Jedynska, et al., Physical and chemical characterisation of PM emissions from two ships operating in European emission control areas, Atmos. Meas. Tech. 6 (2013) 3577–3596.
[23] T. Torvela, J. Tissari, O. Sippula, T. Kaivosoja, J. Leskinen, A. Virén, et al., Effect of wood combustion conditions on the morphology of freshly emitted fine particles, Atmos. Environ. 87 (2014) 65–76.
[24] R. Yoshiie, Y. Taya, T. Ichiyanagi, Y. Ueki, I. Naruse, Emissions of particles and trace elements from coal gasification, Fuel 108 (2013) 67–72.
[25] H. Wiinikka, F. Weiland, E. Pettersson, O. Öhrman, P. Carlsson, J. Stjernberg, Characterisation of submicron particles produced during oxygen blown entrained flow gasification of biomass, Combust. Flame 161 (2014) 1923–1934.
[26] J.B. Howard, W.J. Kausch, Soot controlled by fuel additives, Prog. Energy Combust. Sci. 6 (1980) 263–276.
[27] P.A. Bonczyk, Effect of metal additives on soot precursors and particulates in $C_2H_4/O_2/N_2/Ar$ premixed flames, Fuel 70 (1991) 1403–1411.
[28] M. Tappe, B.S. Haynes, J.H. Kent, The effect of alkali metals on a laminar ethylene diffusion flame, Combust. Flame 92 (1993) 266–273.
[29] J. Simonsson, N.E. Olofsson, H. Bladh, M. Sanati, P.E. Bengtsson, Influence of potassium and iron chloride on the early stages of soot formation studied using imaging LII/ELS and TEM techniques, Proc. Combust. Inst. 36 (2017) 853–860.
[30] J. Simonsson, N.E. Olofsson, A. Hosseinnia, P.E. Bengtsson, Influence of potassium chloride and other metal salts on soot formation studied using imaging LII and ELS, and TEM techniques, Combust. Flame 190 (2018) 188–200.
[31] J.P.A. Neeft, M. Makkee, J.A. Moulijn, Catalysts for the oxidation of soot from diesel exhaust gases. I. An exploratory study, Appl. Catal., B 8 (1996) 57–78.
[32] J. Song, J. Wang, Boehman Al, The role of fuel-born catalysts in diesel particulate oxidation behavior, Combust. Flame 146 (2006) 73–84.
[33] A. Trubetskaya, P.A. Jensen, A.D. Jensen, A.D. Garcia Llamas, K. Umeki, D. Gardini, et al., Effects of several types of biomass fuels on the yield, nanostructure and reactivity of soot from fast pyrolysis at high temperatures, Appl. Energy 171 (2016) 468–482.
[34] K. Umeki, G. Häggström, A. Bach-Oller, K. Kirtania, E. Furusjö, Reduction of tar and soot formation from entrained-flow gasification of woody biomass by alkali impregnation, Energy Fuels 31 (2017) 5104–5110.
[35] A. Bach-Oller, E. Furusjö, K. Umeki, Effect of potassium impregnation on the emission of tar and soot from biomass gasification, Energy Procedia 158 (2019) 619–624.
[36] H. Wiinikka, P. Toth, K. Jansson, R. Molinder, M. Broström, L. Sandström, et al., Particle formation during pressurized entrained flow gasification of wood powder: effects of process conditions on chemical composition, nanostructure, and reactivity, Combust. Flame 189 (2018) 1339–1351.
[37] P. Toth, T. Vikström, R. Molinder, H. Wiinikka, Structure of carbon black continuously produced from biomass pyrolysis oil, Green Chem. 20 (2018) 3981–3992.
[38] T.C. Lovejoy, Q.M. Ramasse, M. Falke, A. Kaeppel, R. Terborg, R. Zan, et al., Single atom identification by energy dispersive x-ray spectroscopy, Appl. Phys. Lett. 100 (2012) 154101.
[39] R.M. Stroud, T.C. Lovejoy, M. Falke, N.D. Bassim, G.J. Corbin, N. Dellby, et al., Individual heteroatom identification with X-ray spectroscopy, Appl. Phys. Lett. 108 (2016) 163101.
[40] R. Brydson (Ed.), Aberration-corrected Analytical Electron Microscopy, first ed., John Wiley and Sons, Ltd, 2011.
[41] R.F. Egerton, Electron Energy-Loss Spectroscopy in the Electron Microscope, second ed., Springer, 1996.
[42] P.E. Batson, N. Dellby, O.L. Krivanek, Sub-ångström resolution using aberration corrected electron optics, Nature 418 (2002) 617–620.
[43] D.A. Muller, L Fitting Kourkoutis, M. Murfitt, J.H. Song, H.Y. Hwang, J. Silcox, et al., Atomic-scale chemical imaging of composition and bonding by aberration-corrected microscopy, Science 319 (2008) 1073–1076.
[44] D. Kepaptsoglou, T.P. Hardcastle, C.R. Seabourne, U. Bangert, R. Zan, J Alexander Amani, et al., Electronic structure modification of ion implanted graphene: the spectroscopic signatures of p- and n-type doping, ACS Nano 9 (2015) 11398–11407.
[45] Q.M. Ramasse, C.R. Seabourne, D.M. Kepaptsoglou, R. Zan, U. Bangert, A.J. Scott, Probing the bonding and electronic structure of single atom dopants in graphene with electron energy loss spectroscopy, Nano Lett. 13 (2013) 4989–4995.
[46] G.M. Ilari, F.S. Hage, Y. Zhang, M.D. Rossell, Q.M. Ramasse, M. Niederberger, et al., Carbon–metal interfaces analyzed by aberration-corrected TEM: how copper and nickel nanoparticles interact with MWCNTs, Micron 72 (2015) 52–58.
[47] Y.C. Lin, P.Y. Teng, P.W. Chiu, K. Suenaga, Exploring the single atom spin state by electron spectroscopy, Phys. Rev. Lett. 115 (2015) 206803.
[48] R. Senga, H.P. Komsa, Z. Liu, K. Hirose-Takai, A.V. Krasheninnikov, K. Suenaga, Atomic structure and dynamic behaviour of truly one-dimansional ionic chains inside carbon nanotubes, Nat. Mater. 13 (2014) 1050–1054.
[49] P.V.C. Medeiros, S. Marks, J.M. Wynn, A. Vasylenko, Q.M. Ramasse, et al., Single-atom scale structural selectivity in Te nanowires encapsulated inside ultranarrow, single-walled carbon nanotubes, ACS Nano 11 (2017) 6178–6185.
[50] K. Al-Qurashi, A.L. Boehman, Impact of exhaust gas recirculation (EGR) on the oxidative reactivity of diesel engine soot, Combust. Flame 155 (2008) 675–695.
[51] M. Knauer, M.E. Schuster, D. Su, R. Schlögl, R. Niessner, N.P. Ivleva, Soot structure and reactivity analysis by Raman microspectroscopy, temperature-programmed oxidation, and high-resolution transmission electron microscopy, J. Phys. Chem. 113 (2009) 13871–13880.
[52] B. Apicella, A. Ciajolo, A. Tregrossi, J. Abrahamson, R.L. Vander Wal, C. Russo, HRTEM and EELS investigations of flame-formed soot nanostructures, Fuel 225 (2018) 218–224.
[53] O.L. Krivanek, N. Dellby, M.F. Murfitt, M.F. Chisholm, T.J. Pennycook, K. Suenaga, et al., Gentle STEM: ADF imaging and EELS at low primary energies, Ultramicroscopy 110 (2010) 935–945.
[54] V.S. Sikarwar, M. Zhao, P. Clough, J. Yao, X. Zhong, M.Z. Memon, et al., An overview of advances in biomass gasification, Energy Environ. Sci. 9 (2016) 2939–2977.
[55] F. Weiland, H. Hedman, M. Marklund, H. Wiinikka, O. Öhrman, R. Gebart,

Pressurized oxygen blown entrained-flow gasification of wood powder, Energy Fuels 27 (2013) 932–941.
[56] F. Weiland, H. Wiinikka, H. Hedman, J. Wennebro, E. Pettersson, R. Gebart, Influence of process parameters on the performance of an oxygen blown entrained flow biomass gasifier, Fuel 153 (2015) 510–519.
[57] M. Watanabe, M. Kanno, D.W. Ackland, C.J. Kiely, D.B. Williams, Applications of electron energy loss spectrometry and energy filtration in an aberration-corrected JEM-2200FS STEM/TEM, Microsc. Mikroanal. 13 (2007) 1264–1265.
[58] www.hremresearch.com.
[59] Z. Zhang, R. Brydson, Z. Aslam, S. Reddy, A. Brown, A. Westwood, et al., Investigating the structure of non-graphitising carbons using electron energy loss spectroscopy in the transmission electron microscope, Carbon 49 (2011) 5049–5063.
[60] E. Kim, S. Agarwal, N. Kim, F.S. Hage, V. Leonardo, A. Gelmi, et al., Bioinspired fabrication of DNA - inorganic hybrid composites using synthetic DNA, ACS Nano 13 (2019) 2888–2900.
[61] B.E. Mironov, H.M. Freeman, A.P. Brown, F.S. Hage, A.J. Scott, A.V.K. Westwood, et al., Electron irradiation of nuclear graphite studied by transmission electron microscopy and electron energy loss spectroscopy, Carbon 83 (2015) 106–117.
[62] K. Nitiputri, Q.M. Ramasse, H. Autefage, C.M. McGilvery, S. Boonrungsiman, N.D. Evans, et al., Nanoanalytical electron microscopy reveals a sequential mineralization process involving carbonate-containing amorphous precursors, ACS Nano 10 (2016) 6826–6835.
[63] P. Toth, A.B. Palotas, E.G. Eddings, R.T. Whitaker, J.S. Lighty, A novel framework for the quantitative analysis of high resolution transmission electron micrographs of soot I. Improved measurement of interlayer spacing, Combust. Flame 160 (2013) 909–919.
[64] P. Toth, A.B. Palotas, E.G. Eddings, R.T. Whitaker, J.S. Lighty, A novel framework for the quantitative analysis of high resolution transmission electron micrographs of soot II. Robust multiscale nanostructure quantification, Combust. Flame 160 (2013) 920–932.
[65] C.R. Shaddix, A.B. Palotas, C.M. Megaridis, M.Y. Choi, N.Y.C. Yang, Soot graphitic order in laminar diffusion flames and a large-scale JP-8 pool fire, Int. J. Heat Mass Tran. 48 (2005) 3604–3614.
[66] S. Shim, R.H. Hurt, N.Y.C. Yang, A methodology for analysis of 002 lattice fringe images and its application to combustion-derived carbons, Carbon 38 (2000) 29–45.
[67] M. Sakai, M.H. Iguma, K. Kondo, T. Aizawa, Nanostructure Analysis of Primary Soot Particles Directly Sampled in Diesel Spray Flame via HRTEM (No. 2012-01-1722), SAE Technical Paper, 2012.
[68] P. Toth, D. Jacobsson, M. Ek, H. Wiinikka, Real-time, in situ, atomic scale observation of soot oxidation, Carbon 145 (2019) 149–160.
[69] K.G. Neoh, J.B. Howard, A.F. Sarofim, Effect of oxidation on the physical structure of soot, in: Symposium (International) on Combustion, vol. 20, Elsevier, 1985.
[70] H. Ghiassi, P. Toth, I.C. Jaramillo, J.S. Lighty, Soot oxidation-induced fragmentation: Part 1: the relationship between soot nanostructure and oxidation-induced fragmentation, Combust. Flame 163 (2016) 951–957, 179-187.
[71] H. Ghiassi, I.C. Jaramillo, P. Toth, J.S. Lighty, Soot oxidation-induced fragmentation: Part 2: experimental investigation of the mechanism of fragmentation, Combust. Flame 163 (2016) 170–178.
[72] L.A.J. Garvie, A.J. Craven, R. Brydson, Use of electron-energy loss near-edge fine structure in the study of minerals, Am. Mineral. 79 (1994) 411–425.
[73] H. Daniels, R. Brydson, B. Rand, A. Brown, Investigation carbonization and graphitization using electron energy loss spectroscopy (EELS) in the transmission electron microscope (TEM), Phil. Mag. 87 (2007) 4073–4092.
[74] Z. Zhang, R. Brydson, Z. Aslam, S. Reddy, A. Brown, A. Westwood, et al., Investigating the structure of non-graphitising carbons using electron energy loss spectroscopy in the transmission electron microscope, Carbon 49 (2011) 5049–5063.
[75] A. Braun, F.E. Huggins, N. Shah, Y. Chen, S. Wirick, S.B. Mun, et al., Advantages of soft X-ray absorption over TEM-EELS for solid carbon studies - a comparative study on diesel soot with EELS and NEXAFS, Carbon 43 (2005) 117–124.
[76] C Laffon P Parent, I. Marhaba, D. Ferry, T.Z. Regier, I.K. Ortega, et al., Nanoscale characterization of aircraft soot: a high-resolution transmission electron microscopy, Raman spectroscopy, X-ray photoelectron and near-edge X-ray absorption spectroscopy study, Carbon 101 (2016) 86–100.
[77] C. Vollmer, D. Kepaptsoglou, J. Leitner, H. Busemann, N.H. Spring, Q.M. Ramasse, et al., Fluid-induced organic synthesis in the solar nebula recorded in extraterrestrial dust from meteorites, Proc. Natl. Acad. Sci. Unit. States Am. 111 (2014) 15338–15343.
[78] A. Steele, L.G. Benning, R. Wirth, S. Siljeström, M.D. Fries, E. Hauri, et al., Organic synthesis on Mars by electrochemical reduction of CO_2, Sci. Adv. 4 (2018) eaat5118.
[79] C. Vollmer, J. Leitner, D. Kepaptsoglou, Q.M. Ramasse, H. Busemann, P. Hoppe, Isotopic compositions, nitrogen functional chemistry, and low-loss electron spectroscopy of complex organic aggregates at the nanometer scale in the carbonaceous chondrite Renazzo, Meteoritics Planet Sci. 55 (2020) 1293–1319.
[80] J.A. Brandes, S. Wirick, C. Jacobsen, Carbon K-edge spectra of carbonate minerals, J. Synchrotron Radiat. 17 (2010) 676–682.
[81] X. Liu, T. Pichler, M. Knupfer, J. Flink, H. Kataura, Electronic properties of potassium-intercalated C_{60} peapods, Phys. Rev. B 69 (2004), 075417.
[82] D. Erbahar, T. Susi, X. Rocquefelte, C. Bittencourt, M. Scardamaglia, P. Blaha, et al., Spectromicroscopy of C_{60} and azafullerene $C_{59}N$: identifying surface absorbed water, Sci. Rep. 6 (2016) 35605.
[83] P. Lindgren, L. Hallis, F.S. Hage, M.R. Lee, J. Parnell, A. Plan, et al., A TEM and EELS study of carbon in a melt fragment from the Gardnos impact structure, Meteoritics Planet Sci. 54 (2019) 2698–2709.
[84] J.B. Howard, J.T. McKinnon, Y. Makarovsky, A.L. Lafleur, M.E. Johnson, Fullerenes C_{60} and C_{70} in flames, Nature 352 (1991) 139–141.
[85] W.J. Grieco, J.B. Howard, L.C. Rainey, J.B. Vander Sande, Fullerenic carbon in combustion-generated soot, Carbon 38 (2000) 597–614.
[86] R.T. DeVol, R.A. Metzler, L. Kabalah-Amitai, B. Pokroy, Y. Politi, A. Gal, et al., Oxygen spectroscopy and polarization-dependent imaging contrast (PIC)-mapping of calcium carbonates minerals and biominerals, J. Phys. Chem. B 118 (2014) 8449–8457.
[87] V. Leon, R. Parret, R. Almairac, L. Alvarez, M.R. Babaa, B.P. Doyle, et al., Spectroscopic study of double-walled carbon nanotube functionalization for preparation of carbon nanotube/epoxy composites, Carbon 50 (2012) 4987–4994.
[88] E. Macias-Sanchez, M.G. Willinger, C.M. Pina, A.G. Checa, Transformation of ACC into argonite and the origin of the nanogranular structure of nacre, Sci. Rep. 7 (2017) 12728.
[89] J. Kruse, P. Leinweber, K.U. Eckhardt, F. Godlinski, Y. Huc, L. Zuinc, Phosphorus $L_{2,3}$-edge XANES: overview of reference compounds, J. Synchrotron Radiat. 16 (2009) 247–259.
[90] A. Strandberg, M. Carlborg, C. Boman, M. Broström, Ash transformation during single-pellet combustion of a silicon-poor woody biomass, Energy Fuels 33 (2019) 7770–7777.
[91] D. Boström, N. Skoglund, A. Grimm, C. Boman, M. Öhman, M. Broström, et al., Ash transformation chemistry during combustion of biomass, Energy Fuels 26 (2012) 85–93.
[92] O.L. Krivanek, T.C. Lovejoy, N. Dellby, T. Aoki, R.W. Carpenter, P. Rez, et al., Vibrational spectroscopy in the electron microscope, Nature 514 (2014) 209–212.
[93] F.S. Hage, D.M. Kepaptsoglou, Q.M. Ramasse, L.J. Allen, Phonon spectroscopy at atomic resolution, Phys. Rev. Lett. 122 (2019), 016103.
[94] F.S. Hage, G. Radtke, D.M. Kepaptsoglou, M. Lazzeri, Q.M. Ramasse, Single-atom vibrational spectroscopy in the scanning transmission electron microscope, Science 367 (2020) 1124–1127.
[95] S.M. Collins, D.M. Kepaptsoglou, J. Hou, C.W. Ashling, G. Radtke, T.D. Bennett, et al., Functional group mapping by electron beam vibrational spectroscopy from nanoscale volumes, Nano Lett. 20 (2020) 1272–1279.